Petroleum Science 23 (2026) 220–235

Contents lists available at ScienceDirect

Petroleum Science

journal homepage: www.keaipublishing.com/en/journals/petroleum-science

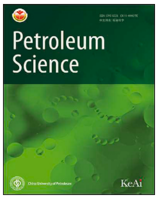

Original Paper

Simulation analysis of hydraulic fracture initiation and propagation mechanisms under mixed-mode and reservoir fracturing

Yu Suo [a,b,c,*], Xian-Hang Wei [a], Yan-Jie Zhao [a], Ying-Jie Wei [a], Shuo Miao [a], Yang Zhao [a], You-Qing Zhu [d], Bin Huang [e]

[a] *Key Laboratory of Enhanced Oil and Gas Recovery, Ministry of Education, Northeast Petroleum University, Daqing, 163318, Heilongjiang, China*
[b] *Postdoctoral Resource Center, Daqing Oilfield Limited Company, Daqing, 163458, Heilongjiang, China*
[c] *Heilongjiang Province Key Laboratory of Oil and Gas Reservoir Fracturing and Evaluation, Daqing, 163318, Heilongjiang, China*
[d] *Daqing Oilfield Downhole Services Company, Daqing, 163458, Heilongjiang, China*
[e] *Chongqing Institute of Unconventional Oil and Gas Development, Chongqing University of Science and Technology, Chongqing, 401331, China*

ARTICLE INFO

Article history:
Received 4 May 2025
Received in revised form
12 September 2025
Accepted 14 September 2025
Available online 19 September 2025

Edited by Jia-Jia Fei

Keywords:
Hydraulic fracturing
Mixed-mode
Fracture propagation
Plastic zone
Perforation spacing optimization

ABSTRACT

With the increasing demand for the development of unconventional oil and gas resources, hydraulic fracturing has become a key technology for enhancing reservoir permeability. However, achieving controlled propagation of fracture networks remains a significant challenge under complex geological conditions. This study integrates theoretical analysis and finite-discrete element method (FDEM) simulations to investigate mixed-mode mechanisms, plastic zone evolution at fracture tips, and anisotropic mechanical responses of shale. Modified fracture criteria-including a T-stress-integrated Mohr-Coulomb criterion and maximum circumferential tensile stress criterion are derived and validated through uniaxial compression and Brazilian splitting tests on Longmaxi Formation shale. Results demonstrate that the modified Mohr-Coulomb criterion effectively predicts anisotropic fracture propagation by characterizing tensile-compressive strength differences, while the plastic zone evolution under maximum circumferential tensile stress is significantly influenced by T-stress: positive T-stress (45°–90°) expands the plastic zone, whereas negative T-stress (0°–45°) contracts it. Lower tensile-to-compressive strength ratios lead to larger plastic zones. An FDEM-based horizontal well fracturing model reveals vertical fracture propagation dominated by bedding plane and interbed fracture extension, forming complex networks, while horizontal fractures initially grow independently before deflecting and interconnecting under maximum principal stress. Sensitivity analysis of perforation spacing identifies 62.5 mm (16 holes/m) as the optimal configuration, achieving Mode II-dominated fracture networks with superior connectivity and stimulation efficiency. Larger spacings (71.4–83.3 mm) result in reduced efficiency or isolated fractures. By coupling stress interference and fluid pressure field dynamics, this study establishes a methodology to balance fracture network complexity and reservoir stimulation efficacy. The findings provide theoretical insights and engineering guidelines for optimizing hydraulic fracturing designs in anisotropic shale gas reservoirs through advanced fracture criteria and FDEM-based multiphysics simulations.

1. Introduction

With rising unconventional hydrocarbon and geothermal energy demands, hydraulic fracturing confronts challenges in fracture control due to reservoir heterogeneity (Li et al., 2025). Natural/artificial fracture interactions and inadequate plastic zone modeling underscore the importance of fracture criteria. Three principal theoretical frameworks exist: strain, stress, and energy

---

* Corresponding author.
E-mail address: sycup09@163.com (Y. Suo).

Peer review under the responsibility of China University of Petroleum (Beijing).

https://doi.org/10.1016/j.petsci.2025.09.025

criteria. Stress criteria predict fracture paths/thresholds via tip stress analysis, energy criteria link plastic energy dissipation to fracture growth, while strain criteria excel in modeling ductile material damage. This study prioritizes stress criteria for their numerical simulation strengths in characterizing fracture initiation/propagation thresholds and tip plastic zone stress distributions.

Stress-based fracture criteria evaluate fracture behaviors through stress analysis, focusing on initiation conditions, propagation paths, and stress interactions. Chen (2013) showed hydraulic fractures deflect along natural fractures, governed by fluid viscosity, injection rate, and stress contrast. Tang et al. (2017) derived critical pressure thresholds with theory-experiment consistency across varied perforation/wellbore parameters. Liu (2019) incorporated T-stress corrections to match experimental initiation angles. Liu et al. (2006) linked fracture angles to loading directions via microcrack models, revealing polyline fractures under compressive-shear stress. Li et al. (2014) quantified mixed-mode angles using fracture features, loading orientation, and friction, noting T-stress effects on circumferential stress extremes. Fracture tip plastic zones dictate failure modes, analyzed via stress/strain simulations to reveal deformation governed by material states, fracture shapes, and loads. Some scholars have also linked fracture toughness to plastic zones via strain criteria, using zone radius as a fracture metric (Aliha et al., 2010; Wei et al., 2017; Wu and Li, 1989). Yang et al. (2017, 2019) showed plastic zones shrink with material thickness in 3D bending, approaching plane strain limits. Liu (2018) categorized fracture criteria by plastic zone assumptions. Sousa et al. (2013) enhanced Irwin's model with T-stress, noting yield-stress ratio impacts. Hu et al. (2010) quantified fracture process zone (FPZ) dimensions via strength ratios and Poisson's ratio. Gao et al. (2021) formulated 2D rock plastic zones using Mohr-Coulomb, assessing angle/parameter interactions with hardening.

Finite element method (FEM) and discrete element method (DEM) remain main numerical tools: FEM uses continuum mechanics for stress analysis but fails to track dynamic fractures and discontinuities. DEM models fracture processes but lacks stress accuracy with high cost. Finite-discrete element method (FDEM) combines both, enabling accurate stress fields and dynamic fracture tracking. It addresses both reservoir-scale stresses and fracture behaviors (initiation/branching/deflection), while handling multi-field coupling and reservoir heterogeneity. FDEM serves as an efficient tool for optimizing fracture networks in shale/geothermal projects. Table 1 compares their strengths.

FEM predicts hydraulic fracture initiation/propagation and stress-fluid interactions through coupled rock-fluid models. Zuo et al. (2025) showed pulse injection boosts fracture dimensions and reduces pressure via ABAQUS, with tensile failure dominance. Zhang et al. (2024) used XFEM to identify stress control, coal-rock thickness effects, and injection rate impacts in roof fracturing, noting initiation sequence dictates fracture size. Cao et al. (2024) modeled dry hot rock reservoirs, highlighting stress, elastic modulus, Poisson's ratio, and temperature as key propagation drivers. Wang S. et al. (2024) validated models through four-stage fracture classification with fiber-optic strain. Xu et al. (2025) studied bedding angles and stress differentials on coal fracture patterns/branching frequency. DEM simulates hydraulic fracture propagation, failure mechanisms, and rock fracturing. Zhang et al. (2025) proposed a fracturing-pressure relief coupling strategy, revealing increased injection rates enhance complex fractures and fracture-bedding interactions. Wang et al. (2021), Zhang et al. (2023) and Wang et al. (2014) optimized initiation pressure formulas via PFC, quantifying stress impacts on fracture growth and multi-factor effects. Fatahi et al. (2017) validated DEM's reliability in sandstone fracturing. Kang et al. (2018) clarified injection parameter and in-situ stress control mechanisms. Li et al. (2019) integrated DEM-DFN modeling to decode fracture network genesis in naturally fractured reservoirs. FDEM coupling model has advanced hydraulic fracture propagation simulations by enabling precise analysis of rock type, in-situ stress, and fracture characteristic influences, though application studies remain limited (Cui and Hou, 2023, 2024a, 2024b). Wang Q. et al. (2024, 2025) investigated natural fracture zones and minor faults in southern Sichuan shale gas reservoirs, demonstrating their significant control on fracture propagation paths and inter-well interference. Yan and Zheng (2016a, 2016b, 2016c) systematically explored multi-dimensional hydraulic fracturing effects through FDEM-Flow: lateral pressure coefficient (λ) regulates initiation pressure and fracture orientation; Adjacent borehole interference governs fracture trajectory while reducing initiation pressure; And material heterogeneity influences fracture branching and propagation patterns.

In summary, existing limitations persist despite progress in fracture criteria and simulations: inadequate characterization of anisotropic media responses, challenges in modeling multi-field coupling/dynamic fracturing in heterogeneous reservoirs with scarce FDEM applications, and insufficient quantitative analysis of perforation spacing impacts. This study addresses these gaps by modifying Mohr-Coulomb and tensile stress criteria to formulate mixed-mode tip plastic zones, validated via shale compression/splitting tests. A shale reservoir FDEM model elucidates vertical/horizontal fracture propagation and perforation spacing's control over network geometry, establishing optimized fracturing strategies for complex reservoirs.

2. Shale strength characterization experiments

This chapter examines the outcrop laminated shale of the Longmaxi Formation in the G area of the Sichuan Basin. The shale's micro-pores mainly consist of organic and inorganic pores. Organic pores, mainly in organic-rich shale (TOC > 2%), are mostly "ink-bottle" shaped and are key for shale gas adsorption and storage. Inorganic pores include intergranular, intragranular,

Table 1
Comparison of FDEM applicability with FEM and DEM.

	FEM	DEM	FDEM
Medium assumption	Continuous medium	Discontinuous medium	Continuous-discontinuous coupled medium
Fracture propagation simulation	Requires predefined path or damage model	Naturally supports dynamic propagation	Dynamic propagation + coupling with continuous stress field
Computational efficiency	High (continuous problem)	Low (when the number of particles is large)	Moderate (need to balance continuous/discontinuous calculations)
Multiphysics coupling functionality	Strong (seepage, temperature field)	Weak (mechanics)	Strong (supports complex coupling)
Application scenarios	Macroscopic stress analysis, homogeneous model	Fragmented rock mass, simple fracture networks	Complex fracture networks, heterogeneous reservoirs

intercrystalline (e.g., clay mineral interlayer pores), and dissolution pores. There are also diagenetic shrinkage fractures, tectonic fractures, and organic matter evolution-induced abnormal pressure fractures.

Mineralogical analysis shows that the Longmaxi Formation shale in the G area mainly contains quartz, carbonate minerals, pyrite, clay minerals, and a few other minerals. The shale has well-developed bedding, mostly continuous layers with some blocky bedding. The average quartz content is 47%, and carbonate minerals are 24%, totaling 71%, which is good for natural fractures and hydraulic fracturing. Pyrite is 1.8%, and clay minerals are 23.4%, mostly illite and illite-smectite interlayers.

2.1. *Uniaxial compression test of laminated shale*

2.1.1. *Sample preparation*

Shale is a typical unconventional reservoir rock, has well-developed structural weak planes like bedding and micro-fractures, leading to significant anisotropy in its mechanical properties. This section focuses on laminated shale, analyzing its anisotropic characteristics under different bedding angles through uniaxial compression tests. Fig. 1 shows the coring methods and samples of various laminated shales. All samples come from the same rock mass to ensure consistent lamination thickness and density. The angle θ between the coring direction and bedding direction is 0°, 30°, 45°, 60°, and 90°. Three samples per type are prepared to avoid test value fluctuations. Sample preparation follows the International Society for Rock Mechanics (ISRM) standards, producing standard cylindrical samples (25 mm diameter, 50 mm height). To minimize rock heterogeneity and randomness, samples are trimmed and polished after coring, with length tolerance $\leq$0.2 mm and end face parallelism $\pm$0.2 mm.

2.1.2. *Strength characterization analysis*

Due to the well-developed bedding in the Longmaxi Formation shale, its uniaxial compressive strength is significantly affected by the coring angle of the shale. As shown in Fig. 2, the uniaxial compressive strength of Longmaxi Formation shale with a 30° bedding angle is slightly lower than that with a 0° bedding angle. The average uniaxial compressive strengths of 0° and 30° bedding shales are 156.39 and 153.53 MPa, respectively. Additionally, there is a sample with a uniaxial compressive strength of 147.31 MPa in the 30° bedding shale. As the bedding angle increases from 30° to 60°, the uniaxial compressive strength of the shale further decreases in an approximately linear trend. When the bedding angle continues to increase to 90°, the compressive strength significantly increases and reaches its maximum value.

The influence of different bedding angles on the elastic modulus of shale is shown in Table 2. As the bedding angle increases from 0° to 45°, the elastic modulus gradually decreases. When the bedding angle increases from 45° to 90°, the elastic modulus increases accordingly. The elastic modulus is the smallest at a 45° bedding angle and the largest at a 90° bedding angle. The uniaxial compression tests reveal that the Longmaxi Formation laminated shale exhibits significant strength anisotropy.

2.2. *Shale Brazilian splitting test*

2.2.1. *Sample preparation*

The coring samples of different laminated shales are shown in Fig. 3. The samples are prepared according to the standards of the ISRM. Disc-shaped samples with dimensions of 50 mm × 25 mm are selected. The parallelism of the upper and lower ends of the samples should be within $\pm$0.05 mm, and the surface flatness should be within $\pm$0.03 mm. To investigate the influence of bedding angle on the anisotropy of mechanical properties and failure modes of shale, samples with different bedding angles are used, including $\theta = 0°$, 30°, 45°, 60°, and 90°.

2.2.2. *Strength characterization analysis*

Fig. 4 shows the tensile strength of laminated shale. It can be observed that the tensile strength of shale decreases gradually with the increase of bedding angle. When the bedding angle is 0°, the tensile strength of shale is the highest, with an average value of about 16.19 MPa. When the bedding angle is 90°, the tensile strength of shale is the lowest, with an average value of about 10.00 MPa. The tensile strength of shale varies significantly, indicating strong anisotropy. The specific experimental data are shown in Table 3.

3. Research on the initiation and propagation of mixed-mode

3.1. *Hydraulic fracture propagation criterion*

3.1.1. *Modified Mohr-Coulomb criterion*

Based on the research content in Section 2, the variation trends of tensile strength and compressive strength are different. The

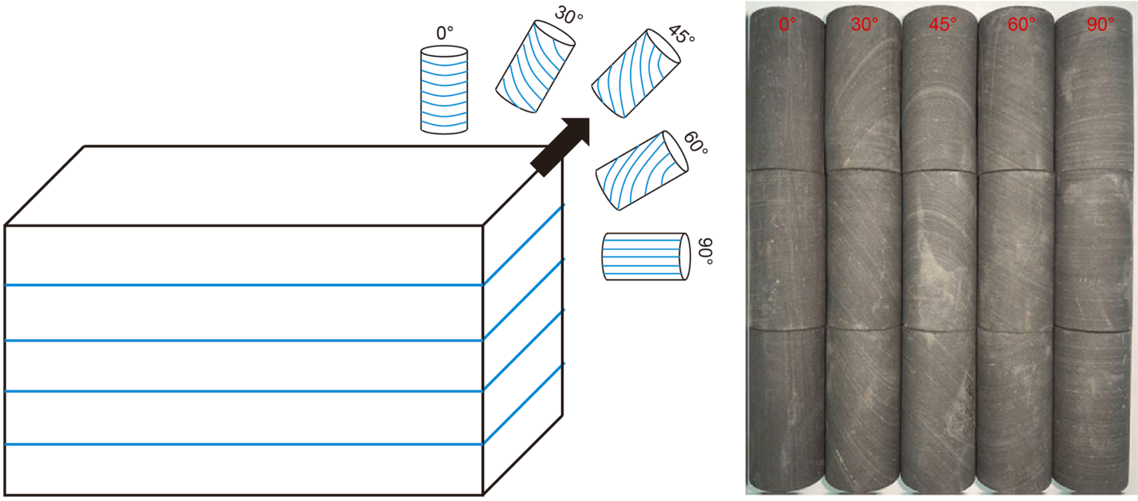

Fig. 1. Coring methods and cylindrical patterns of shale samples at different bedding angles.

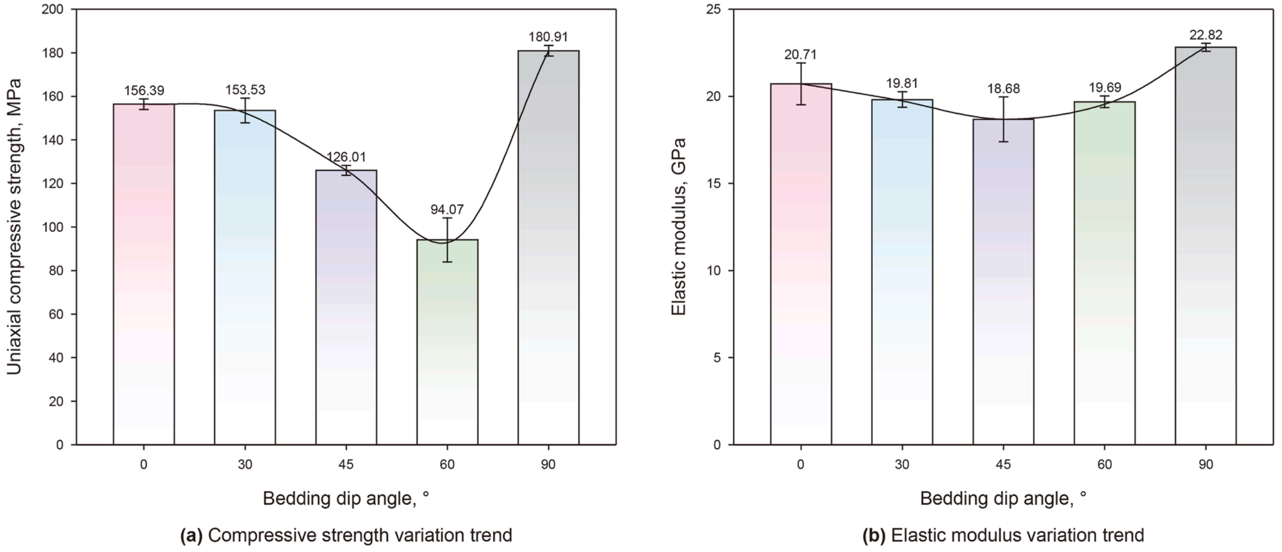

(a) Compressive strength variation trend

(b) Elastic modulus variation trend

Fig. 2. The impact of different bedding angles on shale strength.

Table 2
Experimental data of shale uniaxial compression at different bedding angles.

Bedding angle,°	Core number	Elastic modulus, GPa	Average elastic modulus, GPa	Uniaxial compressive strength, MPa	Average uniaxial compressive strength, MPa
0	S-0-1	19.761		158.94	
	S-0-2	20.307	20.709	154.13	156.39
	S-0-3	22.065		156.11	
30	S-30-1	19.959		147.31	
	S-30-2	20.166	19.812	158.36	153.53
	S-30-3	19.314		154.91	
45	S-45-1	19.086		128.58	
	S-45-2	19.713	18.678	124.64	126.01
	S-45-3	17.235		124.81	
60	S-60-1	20.076		105.31	
	S-60-2	19.548	19.689	85.72	94.07
	S-60-3	19.446		91.19	
90	S-90-1	22.845		183.46	
	S-90-2	23.037	22.818	178.69	180.91
	S-90-3	22.572		180.59	

modified Mohr-Coulomb criterion takes into account the situation where the tensile and compressive strengths of the material are not equal. In light of this, the modified Mohr-Coulomb criterion is used to analyze the failure and fracture behavior of Longmaxi Formation shale.

The modified Mohr-Coulomb criterion takes into account the situation where the tensile and compressive strengths of the material are not equal. The strength criterion established based on this is:

$$\sigma_1 - \frac{\sigma_\mathrm{t}}{\sigma_\mathrm{c}}\sigma_3 = \sigma_\mathrm{t} \tag{1}$$

in the equation, σ_1 is the maximum principal stress, σ_3 is the minimum principal stress, σ_t is the tensile strength of the material, σ_c is the compressive strength of the material.

The local stress at the front of the Mode I-II mixed-mode fracture can be obtained by stress transformation as:

$$\begin{cases} \sigma_{1,3} = \dfrac{\sigma_x + \sigma_y}{2} \pm \sqrt{\left(\dfrac{\sigma_x - \sigma_y}{2}\right)^2 + \tau_{xy}^2} \\ \sigma_2 = \mu(\sigma_1 + \sigma_2) = \mu\left(\sigma_x + \sigma_y\right) \end{cases} \tag{2}$$

in the equation, σ_x is the normal stress in the x-direction, σ_y is the normal stress in the y-direction, τ_{xy} is the shear stress on the x-y plane, μ is Poisson's ratio of the material.

Assuming the length of the hydraulic fracture is L, and the stress intensity factors at the fracture tip are K_I^hf and $K_\mathrm{II}^\mathrm{hf}$, based on linear elastic fracture mechanics, the stress field near the fracture tip is the superposition of the Mode I and Mode II stress fields. Under plane strain conditions, the stress field is given by:

$$\begin{cases} \sigma_x^\mathrm{hf} = \dfrac{K_\mathrm{I}^\mathrm{hf}}{\sqrt{2\pi r}}\cos\dfrac{\theta}{2}\left(1 - \sin\dfrac{\theta}{2}\sin\dfrac{3\theta}{2}\right) - \dfrac{K_\mathrm{II}^\mathrm{hf}}{\sqrt{2\pi r}}\sin\dfrac{\theta}{2}\left(2 + \cos\dfrac{\theta}{2}\cos\dfrac{3\theta}{2}\right) \\ \sigma_y^\mathrm{hf} = \dfrac{K_\mathrm{I}^\mathrm{hf}}{\sqrt{2\pi r}}\cos\dfrac{\theta}{2}\left(1 + \sin\dfrac{\theta}{2}\sin\dfrac{3\theta}{2}\right) + \dfrac{K_\mathrm{II}^\mathrm{hf}}{\sqrt{2\pi r}}\sin\dfrac{\theta}{2}\cos\dfrac{\theta}{2}\cos\dfrac{3\theta}{2} \\ \tau_{xy}^\mathrm{hf} = \dfrac{K_\mathrm{I}^\mathrm{hf}}{\sqrt{2\pi r}}\sin\dfrac{\theta}{2}\cos\dfrac{\theta}{2}\cos\dfrac{3\theta}{2} + \dfrac{K_\mathrm{II}^\mathrm{hf}}{\sqrt{2\pi r}}\cos\dfrac{\theta}{2}\left(1 - \sin\dfrac{\theta}{2}\sin\dfrac{3\theta}{2}\right) \end{cases} \tag{3}$$

in the equation, σ_x^hf is the normal stress in the x-direction at the hydraulic-fracture tip, σ_y^hf is the normal stress in the y-direction at the hydraulic-fracture tip, τ_{xy}^hf is the in-plane shear stress on the x-y

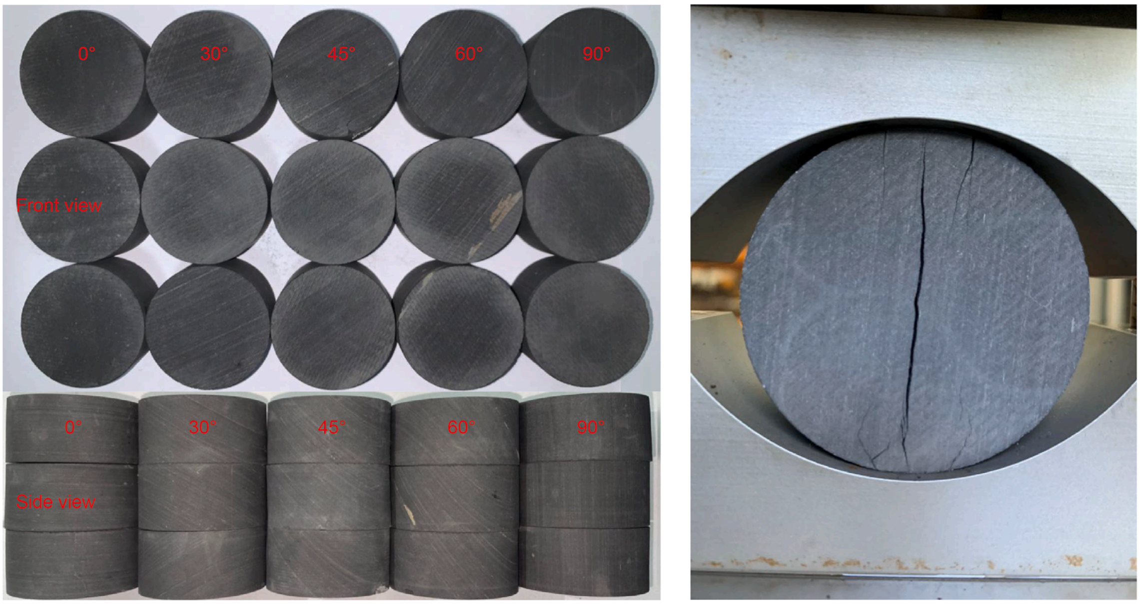

(a) Shale disc specimens with different bedding angles **(b)** Brazilian splitting test

Fig. 3. Experimental specimen diagram.

plane at the hydraulic-fracture tip, $K_{\mathrm{I}}^{\mathrm{hf}}$ is the Mode I stress-intensity factor of the hydraulic fracture, $K_{\mathrm{II}}^{\mathrm{hf}}$ is the Mode II stress-intensity factor of the hydraulic fracture, r is the radial distance from the fracture tip to the point of interest, θ is the polar angle measured between the line connecting the fracture surface to the point of interest and the fracture extension line.

Substituting Eq. (3) into Eq. (2), the local stress at the front of the Mode I-II mixed-mode fracture, expressed in terms of the stress intensity factors, is obtained as:

$$\begin{cases} \sigma_1 = \dfrac{1}{\sqrt{2\pi r}}\left[\left(K_{\mathrm{I}}^{\mathrm{hf}}\cos\dfrac{\theta}{2} - K_{\mathrm{II}}^{\mathrm{hf}}\sin\dfrac{\theta}{2}\right) + \dfrac{1}{2}\sqrt{\left(K_{\mathrm{I}}^{\mathrm{hf}}\sin\theta + 2K_{\mathrm{II}}^{\mathrm{hf}}\cos\theta\right)^2 + \left(K_{\mathrm{II}}^{\mathrm{hf}}\sin\theta\right)^2}\right] \\ \sigma_3 = \dfrac{1}{\sqrt{2\pi r}}\left[\left(K_{\mathrm{I}}^{\mathrm{hf}}\cos\dfrac{\theta}{2} - K_{\mathrm{II}}^{\mathrm{hf}}\sin\dfrac{\theta}{2}\right) - \dfrac{1}{2}\sqrt{\left(K_{\mathrm{I}}^{\mathrm{hf}}\sin\theta + 2K_{\mathrm{II}}^{\mathrm{hf}}\cos\theta\right)^2 + \left(K_{\mathrm{II}}^{\mathrm{hf}}\sin\theta\right)^2}\right] \\ \sigma_2 = \dfrac{2\mu}{\sqrt{2\pi r}}\left(K_{\mathrm{I}}^{\mathrm{hf}}\cos\dfrac{\theta}{2} - K_{\mathrm{II}}^{\mathrm{hf}}\sin\dfrac{\theta}{2}\right) \end{cases} \tag{4}$$

Let α represent the ratio of the tensile strength to the uniaxial compressive strength of the rock. $\alpha = \sigma_{\mathrm{t}}/\sigma_{\mathrm{c}}$, substituting Eq. (4) into Eq. (1) gives the length r of the plastic zone at the tip of the hydraulic fracture, as shown in Eq. (5):

$$r = \frac{1}{2\pi\sigma_{\mathrm{t}}^2}\left[\begin{array}{c}(1-\alpha)\cdot\left(K_{\mathrm{I}}^{\mathrm{hf}}\cos\dfrac{\theta}{2} - K_{\mathrm{II}}^{\mathrm{hf}}\sin\dfrac{\theta}{2}\right) \\ +\dfrac{(1+\alpha)}{2}\sqrt{\left(K_{\mathrm{I}}^{\mathrm{hf}}\sin\theta + 2K_{\mathrm{II}}^{\mathrm{hf}}\cos\theta\right)^2 + \left(K_{\mathrm{II}}^{\mathrm{hf}}\sin\theta\right)^2}\end{array}\right]^2 \tag{5}$$

3.1.2. *Maximum circumferential tensile stress criterion*

Erdogan and Sih (1963) proposed the maximum tensile stress (MTS) criterion based on the experimental results of pure Mode II fracture propagation. This criterion is applicable to the problem of mixed-mode fracture propagation in brittle materials. The criterion mainly includes two aspects: the direction of fracture propagation is the direction of the maximum circumferential tensile stress; when the circumferential stress in this direction reaches a critical value, the fracture begins to propagate unstably.

When the hydraulic fracture propagates along the direction of the maximum circumferential tensile stress according to the maximum circumferential tensile stress criterion, the equation satisfies Eq. (6):

$$\frac{\partial\sigma_{\theta\theta}}{\partial\theta} = 0, \frac{\partial^2\sigma_{\theta\theta}}{\partial\theta^2} < 0 \tag{6}$$

in the equation, $\sigma_{\theta\theta}$ is the hoop stress in polar coordinates.

When the hydraulic fracture propagates along the direction of the maximum circumferential tensile stress and the

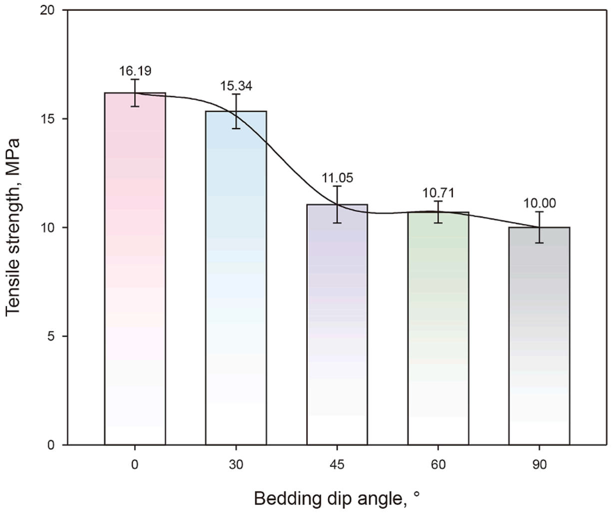

Fig. 4. Tensile strength and error of bedding shale.

Table 3
Data of shale fracturing experiment in Brazil under different bedding angles.

Bedding angle,°	Core number	Peak load, kN	Tensile strength, MPa	Average tensile strength, MPa
0	BD-0-1	30.74	15.66	
	BD-0-2	33.14	16.88	16.19
	BD-0-3	31.45	16.03	
30	BD-30-1	31.39	15.99	
	BD-30-2	28.38	14.46	15.34
	BD-30-3	30.53	15.56	
45	BD-45-1	20.01	10.19	
	BD-45-2	21.78	11.09	11.05
	BD-45-3	23.31	11.88	
60	BD-60-1	21.95	11.18	
	BD-60-2	19.98	10.18	10.71
	BD-60-3	21.12	10.76	
90	BD-90-1	21.24	10.82	
	BD-90-2	19.07	9.72	10.00
	BD-90-3	18.59	9.47	

circumferential stress in this direction reaches a critical value according to the maximum circumferential tensile stress criterion, the fracture begins to propagate unstably. This can be expressed as:

$$(\sigma_{\theta\theta})_{\max} = (\sigma_{\theta\theta})_{\mathrm{c}} = \sigma_{\mathrm{t}} \tag{7}$$

Transforming Eq. (3) into the stress field near the fracture tip in polar coordinates:

$$\begin{cases} \sigma_{\mathrm{rr}} = \dfrac{1}{2\sqrt{2\pi r}}\left[K_{\mathrm{I}}^{\mathrm{hf}}(3-\cos\theta)\cos\dfrac{\theta}{2} + K_{\mathrm{II}}^{\mathrm{hf}}(3\cos\theta - 1)\sin\dfrac{\theta}{2}\right] \\ \sigma_{\theta\theta} = \dfrac{1}{2\sqrt{2\pi r}}\cos\dfrac{\theta}{2}\left[K_{\mathrm{I}}^{\mathrm{hf}}(1+\cos\theta) - 3K_{\mathrm{II}}^{\mathrm{hf}}\sin\theta\right] \\ \tau_{\mathrm{r}\theta} = \dfrac{1}{2\sqrt{2\pi r}}\cos\dfrac{\theta}{2}\left[K_{\mathrm{I}}^{\mathrm{hf}}\sin\theta + K_{\mathrm{II}}^{\mathrm{hf}}(3\cos\theta - 1)\right] \end{cases} \tag{8}$$

in the equation, σ_{rr} is the radial stress in polar coordinates, $\tau_{\mathrm{r}\theta}$ is the radial–hoop shear stress in polar coordinates.

Substituting Eq. (8) into Eq. (7), the length of the plastic zone at the tip of the hydraulic fracture under the maximum circumferential tensile stress criterion can be obtained:

$$r = \frac{1}{8\pi\sigma_{\mathrm{t}}^2}\left\{\cos\frac{\theta}{2}\left[K_{\mathrm{I}}^{\mathrm{hf}}(1+\cos\theta) - 3K_{\mathrm{II}}^{\mathrm{hf}}\sin\theta\right]\right\}^2 \tag{9}$$

3.1.3. *Maximum circumferential tensile stress criterion considering T-stress*

Traditional linear elastic fracture mechanics considers that the stress field near the fracture tip is determined by the singular term represented by the stress intensity factor, thus the stress field near the fracture tip only considers the singular term of the stress intensity factor and neglects the non-singular term. The non-singular term mainly refers to the stress that has a significant impact on fracture propagation when the transverse load and the lateral load on the fracture are not equal, i.e., the T-stress. Cotterell and Rice (1980) have shown that under certain conditions, T-stress has a significant effect on the Mode I fracture toughness and the fracture propagation angle. Similarly, T-stress also has a significant influence on the propagation path and fracture toughness value of Mode I-II mixed-mode fracture. Therefore, when the hydraulic fracture is subjected to the minimum horizontal stress (σ_{h}) and the maximum horizontal stress (σ_{H}), the expression of its tip stress field in the Cartesian coordinate system should be rewritten as:

$$\begin{cases} \sigma_x^{\mathrm{hf}} = \dfrac{K_{\mathrm{I}}^{\mathrm{hf}}}{\sqrt{2\pi r}}\cos\dfrac{\theta}{2}\left(1-\sin\dfrac{\theta}{2}\sin\dfrac{3\theta}{2}\right) - \dfrac{K_{\mathrm{II}}^{\mathrm{hf}}}{\sqrt{2\pi r}}\sin\dfrac{\theta}{2}\left(2+\cos\dfrac{\theta}{2}\cos\dfrac{3\theta}{2}\right) + T \\ \sigma_y^{\mathrm{hf}} = \dfrac{K_{\mathrm{I}}^{\mathrm{hf}}}{\sqrt{2\pi r}}\cos\dfrac{\theta}{2}\left(1+\sin\dfrac{\theta}{2}\sin\dfrac{3\theta}{2}\right) + \dfrac{K_{\mathrm{II}}^{\mathrm{hf}}}{\sqrt{2\pi r}}\sin\dfrac{\theta}{2}\cos\dfrac{\theta}{2}\cos\dfrac{3\theta}{2} \\ \tau_{xy}^{\mathrm{hf}} = \dfrac{K_{\mathrm{I}}^{\mathrm{hf}}}{\sqrt{2\pi r}}\sin\dfrac{\theta}{2}\cos\dfrac{\theta}{2}\cos\dfrac{3\theta}{2} + \dfrac{K_{\mathrm{II}}^{\mathrm{hf}}}{\sqrt{2\pi r}}\cos\dfrac{\theta}{2}\left(1-\sin\dfrac{\theta}{2}\sin\dfrac{3\theta}{2}\right) \end{cases} \tag{10}$$

Transforming Eq. (1) into the stress field near the fracture tip in polar coordinates:

$$\begin{cases} \sigma_{\mathrm{rr}}^{\mathrm{hf}} = \dfrac{1}{2\sqrt{2\pi r}}\left[K_{\mathrm{I}}^{\mathrm{hf}}(3-\cos\theta)\cos\dfrac{\theta}{2} + K_{\mathrm{II}}^{\mathrm{hf}}(3\cos\theta-1)\sin\dfrac{\theta}{2}\right] + T\cos^2\theta \\ \sigma_{\theta\theta}^{\mathrm{hf}} = \dfrac{1}{2\sqrt{2\pi r}}\cos\dfrac{\theta}{2}\left[K_{\mathrm{I}}^{\mathrm{hf}}(1+\cos\theta) - 3K_{\mathrm{II}}^{\mathrm{hf}}\sin\theta\right] + T\sin^2\theta \\ \tau_{\mathrm{r}\theta}^{\mathrm{hf}} = \dfrac{1}{2\sqrt{2\pi r}}\cos\dfrac{\theta}{2}\left[K_{\mathrm{I}}^{\mathrm{hf}}\sin\theta + K_{\mathrm{II}}^{\mathrm{hf}}(3\cos\theta-1)\right] - T\sin\theta\cos\theta \end{cases} \tag{11}$$

in the equation, $T = -(\sigma_{\mathrm{H}} - \sigma_{\mathrm{h}})\cos 2\beta$, where β is the angle between the hydraulic fracture and the direction of the minimum horizontal principal stress.

When the hydraulic fracture propagates along the direction of the maximum circumferential tensile stress according to the maximum circumferential tensile stress criterion, the equation satisfies Eq. (6). Solving Eqs. (12) and (13) will yield the propagation angle $\theta_{\max}$ of the hydraulic fracture.

$$\left.\frac{\partial\sigma_\theta}{\partial\theta}\right|_{\theta=\theta_{\max}} = -\frac{3}{4\sqrt{2\pi r_{\mathrm{c}}}}\cos\frac{\theta_{\max}}{2}\left[\begin{array}{c} K_{\mathrm{I}}^{\mathrm{hf}}\sin\theta_{\max} \\ +K_{\mathrm{II}}^{\mathrm{hf}}(3\cos\theta_{\max}-1) \end{array}\right] + T\sin 2\theta_{\max} = 0 \tag{12}$$

$$\frac{\partial^2 \sigma_\theta}{\partial \theta^2}\Big|_{\theta=\theta_{\max}} = \frac{3}{8\sqrt{2\pi r_c}} \left\{ \begin{array}{l} \sin\frac{\theta_{\max}}{2}\left[K_{\mathrm{I}}^{\mathrm{hf}}\sin\theta_{\max} + K_{\mathrm{II}}^{\mathrm{hf}}(3\cos\theta_{\max}-1)\right] \\ -2\cos\frac{\theta_{\max}}{2}\left(K_{\mathrm{I}}^{\mathrm{hf}}\cos\theta_{\max} - 3K_{\mathrm{II}}^{\mathrm{hf}}\sin\theta_{\max}\right) \end{array} \right\} + 2T\cos 2\theta_{\max} \tag{13}$$

in the equation, r_c is defined as the critical distance ahead of the crack tip, which is used to determine the direction of the maximum hoop tensile stress and is generally assigned a value of an infinitesimal distance close to the crack tip.

At the same time, when the hydraulic fracture has not yet occurred, the length of the plastic zone at the tip of the hydraulic fracture under the maximum circumferential tensile stress criterion, considering the T-stress, is given by:

$$r = \frac{1}{8\pi\sigma_t^2}\left\{\cos\frac{\theta}{2}\left[K_{\mathrm{I}}^{\mathrm{hf}}(1+\cos\theta) - 3K_{\mathrm{II}}^{\mathrm{hf}}\sin\theta\right] + T\sin^2\theta\right\}^2 \tag{14}$$

3.2. Plastic zone at the tip of hydraulic fractures under different conditions

Based on the formulas for the plastic zone at the fracture tip proposed in Section 3.1 under the three fracture criteria, the plastic deformation range at the fracture tip under different conditions can be studied through mathematical calculations.

In order to conduct the study, a uniform shale block with a consistent coring orientation was selected. The shale samples were machined into semicircular specimens for the three-point bending tests. The selected shale was non-laminated. The pre-crack angles β were set at 0°, 15°, 30°, and 45°, respectively. The pre-crack width was approximately 1 mm. The specimen radius R was 36 mm, the thickness B was 30 mm, the crack length a was 11 mm, and the spacing between the two bottom supports $2S$ was 60 mm.

Subsequently, the experimental data were utilized to investigate the effects of compound fracture, the tensile-compressive strength ratio, and the T-stress on the plastic zone at the crack tip. By analyzing the extent of the plastic zone, the deformation mechanism of the fracture tip under various geological environments can be revealed, and the impact of the plastic zone on the stability of fracture propagation can be clarified. This process can determine whether the fracture will propagate along the expected path or deviate from the predetermined direction due to the characteristics of the strata, thereby improving the accuracy of fracture control.

3.2.1. The influence of mixed-mode on the plastic zone at the fracture tip

The equations for the plastic zone radius at the fracture tip derived from different fracture criteria (Eqs. (5), (9) and (14)) can be used to determine the plastic zone at the fracture tip. The calculation parameters refer to the basic parameters obtained from the laboratory experiments in Section 2: tensile strength is 16.19 MPa, tensile-to-compressive strength ratio is 0.1, and the differential stress is 3 MPa.

Fig. 5 displays the plastic zone range at the fracture tip under three criteria: MCTS, MCTS with T-stress, and modified Mohr-Coulomb. For both pure Mode I and Mode I-II mixed-mode fractures, the MCTS criterion yields a larger plastic zone than the modified Mohr-Coulomb criterion. When considering T-stress in the MCTS criterion, which factors in σ_{H}, σ_{h}, and fracture angle, the plastic zone increases with positive T-stress and decreases with negative T-stress.

The MCTS criterion predicts a larger plastic zone than the modified Mohr-Coulomb criterion due to differences in failure mechanisms and stress field characteristics. The MCTS criterion, based on tensile-dominated fracture mechanics, uses circumferential tensile stress reaching the material's tensile strength as the failure criterion. The plastic zone extent is determined by the distribution of this tensile stress field, especially under mixed-mode fracture conditions where the Mode II component causes tensile stress to exceed the critical value over a broader range. In contrast, the modified Mohr-Coulomb criterion is based on a combined compressive-shear failure mechanism. The high compressive-to-tensile strength ratio ($\sigma_c \gg \sigma_t$) in its formula restricts plastic zone expansion, and the linear relationship between principal stresses (σ_1 and σ_3) limits the prediction of tensile-dominated regions. Experimental validation shows that shale anisotropy (e.g., tensile strength perpendicular to bedding plane at 10 MPa, compressive strength at 180.91 MPa) amplifies the MCTS criterion's predictive advantage. Fig. 5 confirms that under mixed-mode conditions, the MCTS criterion predicts a plastic zone radius 20%–30% larger than the modified Mohr-Coulomb criterion, highlighting its applicability for analyzing tensile-dominated brittle fractures.

Fig. 5(a) shows that in pure Mode I fracture, the plastic zone at the fracture tip is symmetrically distributed above and below the 0°–180° axis. The hydraulic fracture propagates along the initial direction (0°). With Mode I-II mixed-mode fracture, as Mode I decreases and Mode II increases, the plastic zone symmetry becomes unbalanced. The entire plastic zone rotates clockwise, shrinking the upper region and expanding the lower region, consistent with the transition from Mode I to Mode II.

3.2.2. The influence of tensile-to-compressive strength ratio on the plastic zone at the fracture tip

Based on the indoor experimental data, the average tensile strength and average compressive strength of shale were obtained for five different bedding angles, and the corresponding tensile-to-compressive strength ratios were calculated. From Table 4, it can be seen that the tensile-to-compressive strength ratios for the four bedding angles of 0°, 30°, 45°, and 60° are all around 0.1, while the ratio for the 90° bedding angle is significantly lower, with a value of 0.06. From Tables 5 and 6, it can be seen that in this section's analysis, to study the plastic zone at the fracture tip, two different tensile-to-compressive strength ratios, 0.06 and 0.1, were selected for calculation.

Fig. 6 shows the plastic zone at the fracture tip of shale under different tensile-to-compressive strength ratios. As the tensile-to-compressive strength ratio of shale increases, the outline of the plastic zone at the fracture tip gradually decreases. An increase in the tensile-to-compressive strength ratio indicates that the material's tensile strength has been enhanced relative to its compressive strength. The improvement in tensile strength can alleviate the stress concentration at the fracture tip, thereby reducing the plastic deformation zone at the fracture tip.

3.2.3. The influence of T-stress on the plastic zone at the fracture tip

Fig. 7 illustrates the distribution of the plastic zone at the fracture tip under different angles between the hydraulic fracture and the minimum horizontal stress. When the angle between the hydraulic fracture and the direction of the minimum horizontal stress is 0°, the fracture is subjected to pure Mode I (opening) stress, and the T-stress is zero. As the orientation of the hydraulic fracture changes, the range of the plastic zone at the fracture tip is calculated. It can be seen from Fig. 7 that when the angle between the hydraulic fracture and the minimum horizontal stress is between 45° and 90°, the T-stress is positive, and the range of the plastic zone at the fracture tip gradually increases with the increase of the angle. This trend is observed in both Mode I fractures and Mode I-II mixed-mode fractures. First, as the angle increases,

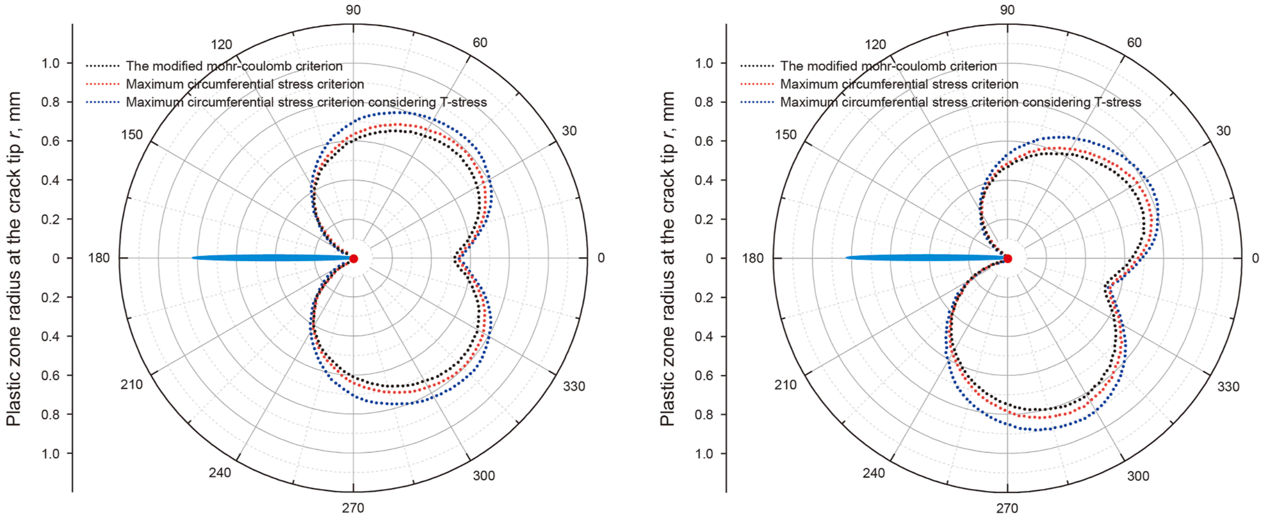

(a) Predefined deflection angle β = 0° (b) Predefined deflection angle β = 15°

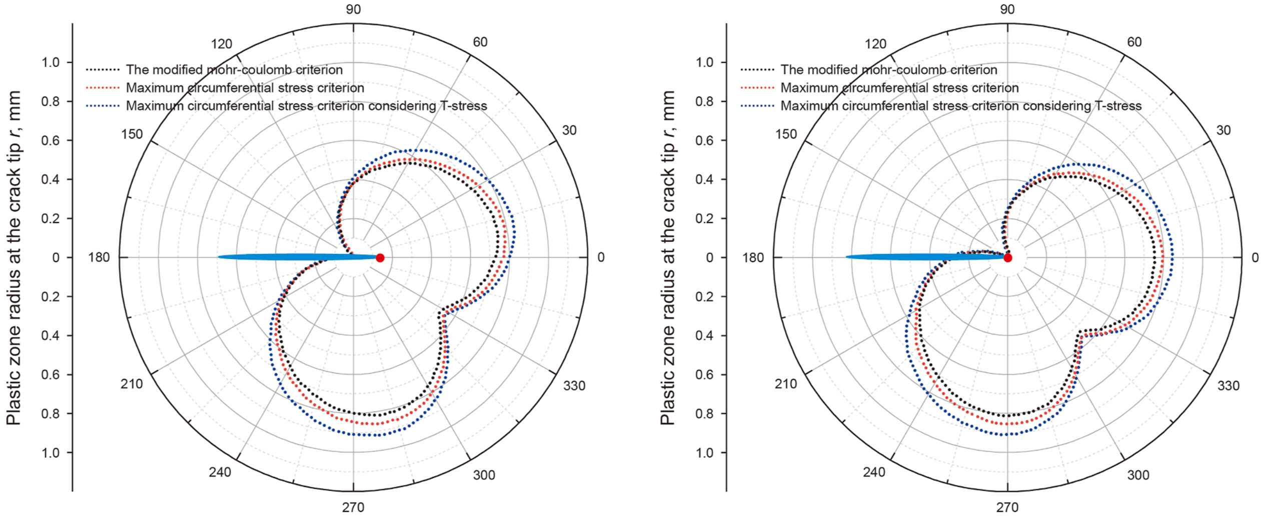

(c) Predefined deflection angle β = 30° (d) Predefined deflection angle β = 45°

Fig. 5. Plastic region of fracture tip under Mode I fracture and I-II mixed-mode.

Table 4
Tensile compression ratio at different bedding angles.

Bedding angle,°	Average tensile strength, MPa	Average compressive strength, MPa	Tensile-to-compressive strength ratio
0	16.19	156.39	0.10
30	15.34	153.53	0.10
45	11.05	126.01	0.09
60	10.71	94.07	0.11
90	10.00	180.91	0.06

Table 5
Initiation pressure error analysis.

Perforation number	Simulated initiation pressure, MPa	Theoretical value, MPa	Absolute error, MPa	Relative error, %
P1	98.5	98.3	0.2	0.20
P2	98.8		0.5	0.51
P3	99.2		0.9	0.92
P4	99.5		1.2	1.22
P5	99.9		1.6	1.63

Table 6
Initiation pressure error analysis.

Perforation number	Simulated initiation pressure, MPa	Theoretical value, MPa	Absolute error, MPa	Relative error, %
P1	98.6	98.3	0.3	0.31
P2	98.9		0.6	0.61
P3	99.2		0.9	0.92
P4	99.5		1.2	1.22
P5	99.8		1.5	1.53

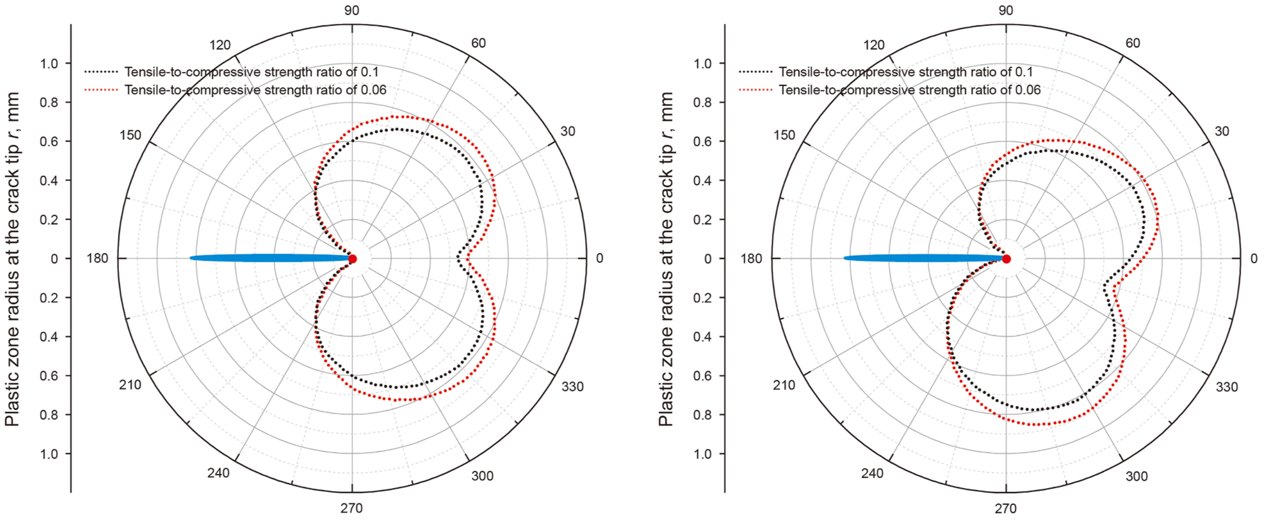

(a) Predefined deflection angle β = 0° **(b)** Predefined deflection angle β = 15°

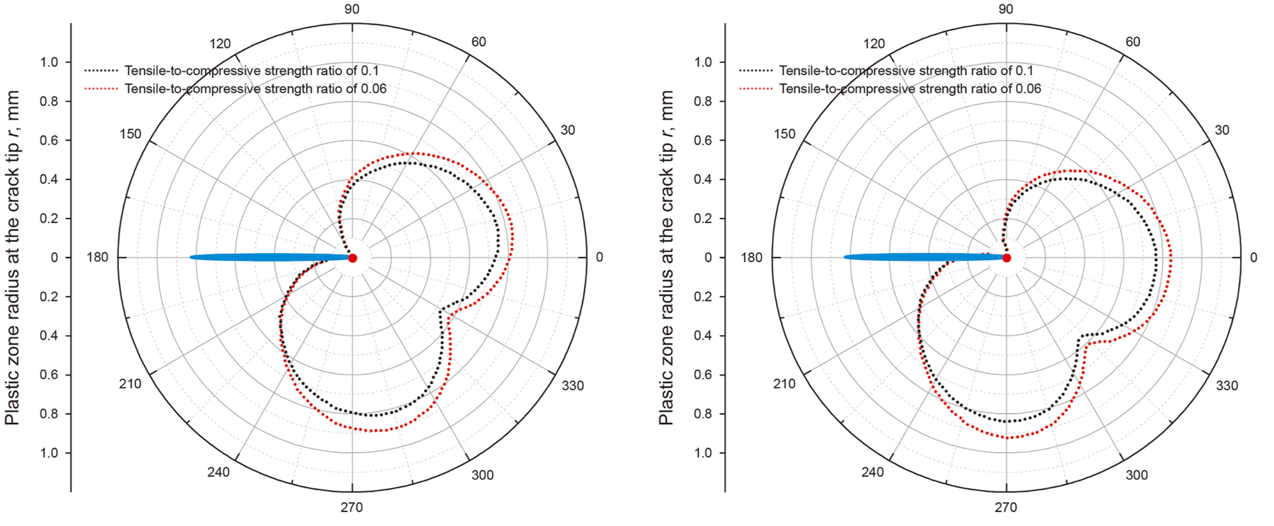

(c) Predefined deflection angle β = 30° **(d)** Predefined deflection angle β = 45°

Fig. 6. Plastic region of crack tip with different tension/compression ratio under Mode I fracture and I-II mixed-mode.

the fracture is not only subjected to opening stress but also generates shear stress components. The superposition of these stress components significantly enhances the stress concentration at the fracture tip, thereby expanding the plastic zone. In addition, the T-stress, as a non-singular stress component at the fracture tip, increases with the angle, further altering the stress field distribution at the fracture tip, intensifying the stress concentration effect, and leading to the expansion of the plastic deformation zone. When the angle between the hydraulic fracture and the minimum horizontal stress is between 0° and 45°, the T-stress is negative, and the range of the plastic zone at the fracture tip decreases with the increase of the T-stress.

4. Numerical simulation study on fracturing application in horizontal well sections of laminated shale reservoirs

4.1. Brief description of simulation scenarios

Well H is located in the G area of the Sichuan Basin, targeting the Longmaxi Formation of the Silurian System, with a well section

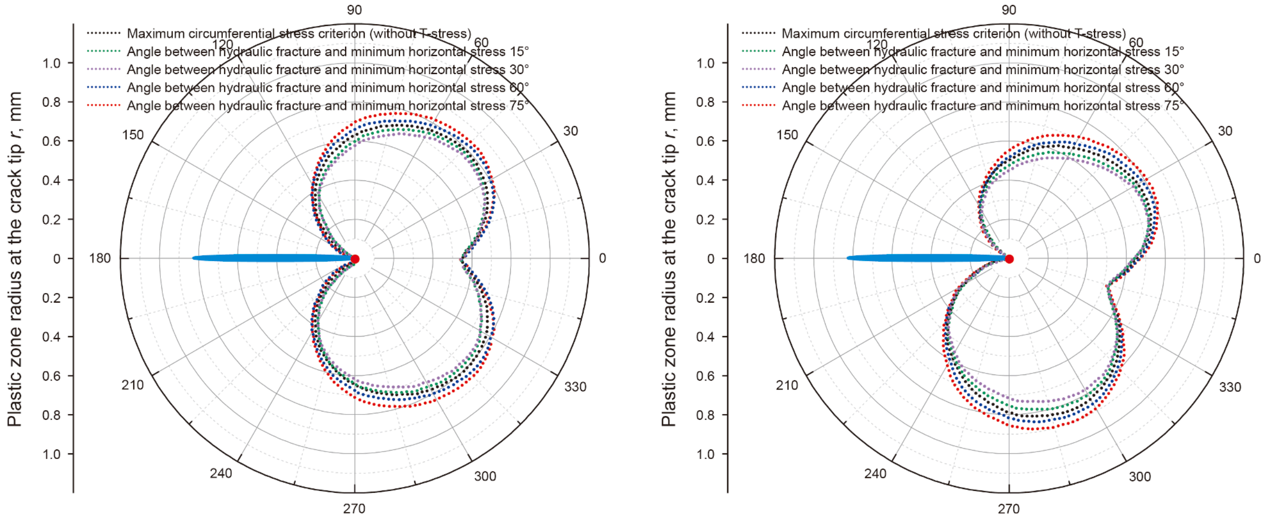

(a) Predefined deflection angle β = 0°

(b) Predefined deflection angle β = 15°

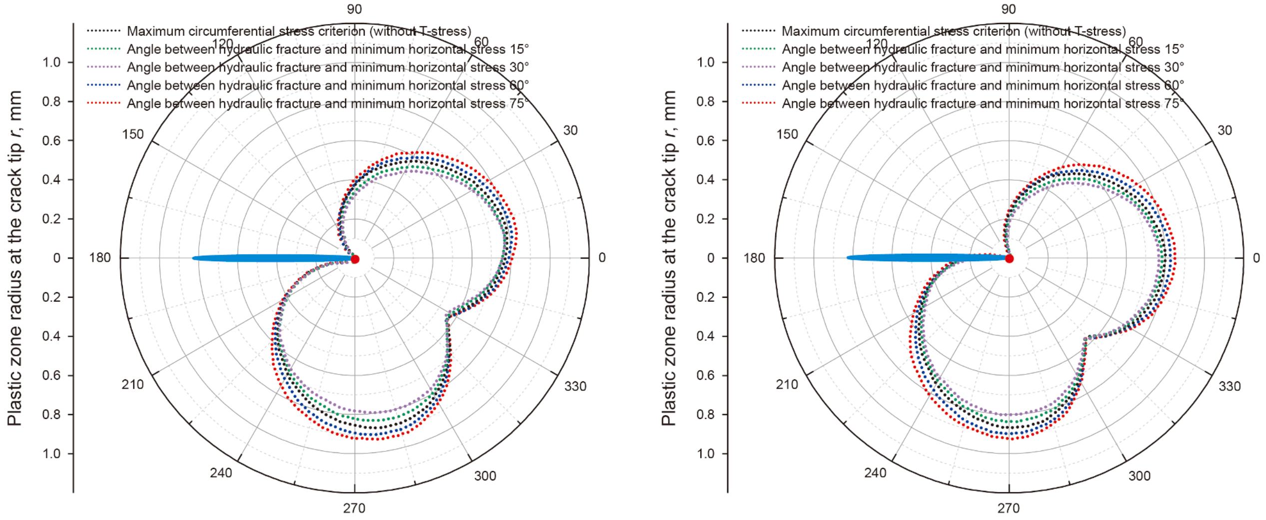

(c) Predefined deflection angle β = 30°

(d) Predefined deflection angle β = 45°

Fig. 7. Plastic region of fracture tip under the angle between different hydraulic fractures and minimum horizontal stress under Mode I fracture and I-II mixed-mode.

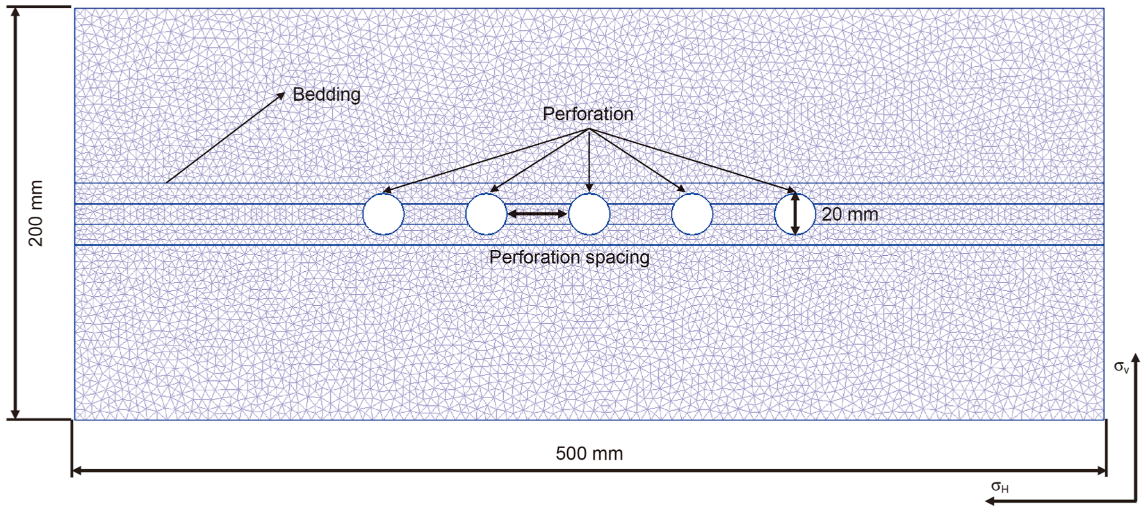

Fig. 8. Numerical model of the vertical profile of staged fracturing of horizontal wells in shale formations.

ranging from 3130 to 4329.9 m. It is a horizontal development well. The regional strata are mainly composed of horizontally laminated shale. The lithology of the Longmaxi Formation primarily consists of gray-black shale, calcareous mudstone, and fine sandstone. Natural fractures are well-developed, mainly in the form of mesh-like and high-angle fractures, filled with calcite and pyrite. The reservoir properties of the Longmaxi Formation are characterized by total porosity ranging from 4.65% to 7.65% (Longyuan I Member) and 2.54%–6.30% (Longyuan II Member), with gas-filled porosity ranging from 2.09% to 4.41%. The permeability ranges from 41.3 to 379 nD (Longyuan I Member) to 111 nD (Longyuan II Member). The average quartz content is 45%, carbonate rock 29%, pyrite 1.6%, with a total brittle mineral content of 77.5% and clay minerals accounting for 21.8% (mainly illite and illite-montmorillonite interlayers). The Young's modulus of the horizontal section of Well H is 25065.9 MPa, with a Poisson's ratio of 0.234, tensile strength of 6.30 MPa, differential horizontal stress of 14.29 MPa, and a fracturability index of 50–60, indicating high reservoir brittleness, which is favorable for the formation of a complex fracture network. The average Mode I fracture toughness of the horizontal section is 1.21 $\text{MPa}\cdot\text{m}^{1/2}$, and the average Mode II fracture toughness is 0.91 $\text{MPa}\cdot\text{m}^{1/2}$. The maximum horizontal principal stress direction is nearly east-west (105°), and the stress state is conducive to the lateral propagation of fractures. The fractures are mainly mesh-like and high-angle fractures, filled with calcite, pyrite, and minor amounts of quartz.

The main mechanical parameters provided by the exploration data are consistent with the ranges of these parameters obtained in this paper, which indicates the strong reliability of the research objects and results of this study. These engineering parameters will be utilized in this paper to simulate the morphology and distribution characteristics of hydraulic fractures in the fractured rock mass.

4.2. The propagation and distribution of hydraulic fractures in the vertical direction of shale reservoirs

4.2.1. Establishment of numerical models

The FDEM is a numerical simulation technique first proposed by Munjiza (2004) in 2004, which integrates the advantages of the finite element method and the discrete element method. In FDEM, a two-dimensional solid medium is discretized into a series of triangular elements. Nodal elements with bonding effects and zero initial thickness are inserted between adjacent triangular elements. This approach allows for the modeling of discontinuous regions in the medium. The constant-strain triangular elements characterize the deformation of the solid, while fracture propagation is simulated through the failure of joint elements.

As shown in Fig. 8, this study employs a two-dimensional numerical model based on a horizontal well located in the vertical section of the shale layer. This model primarily analyzes the shape and characteristics of hydraulic fractures propagating in the plane perpendicular to the rock layer. To enhance computational efficiency, the model size is set to 200 mm × 500 mm, with refined discretization of the bedding planes. The focus of the study is on the extension shape and interconnection of hydraulic fractures between perforations; therefore, other non-target parts are simplified, and only the bedding planes near the perforations are established. The perforation diameter remains at 20 mm, and the initial perforation spacing is set to 50 mm (20 perforations per meter). The matrix parameters of the model are consistent with the given working conditions, and the strength parameters of the bedding planes are set to half of the matrix strength. The model's geostress state is a constant value, with the vertical geostress set to 52 MPa, the maximum horizontal geostress to 55 MPa, and the minimum horizontal geostress to 41 MPa, resulting in an average horizontal geostress of 48 MPa. The pressure value of the

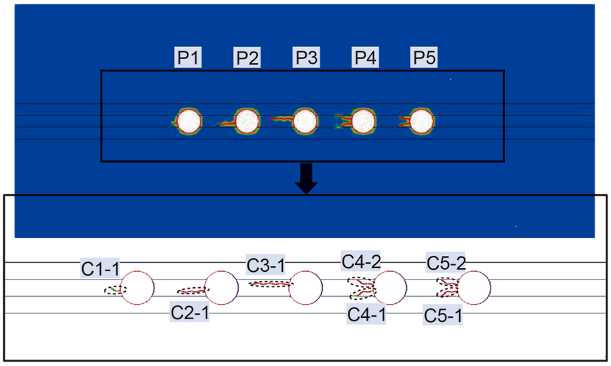

(a) Fracturing stage 1

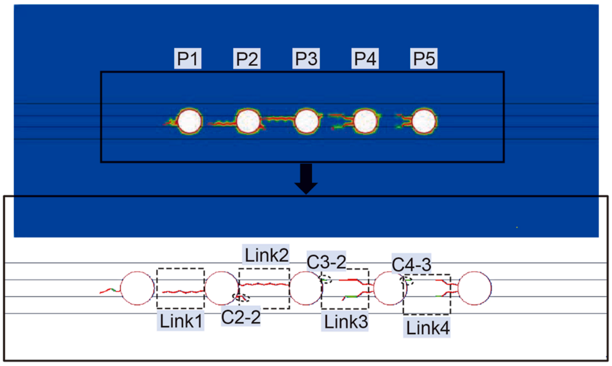

(b) Fracturing stage 2

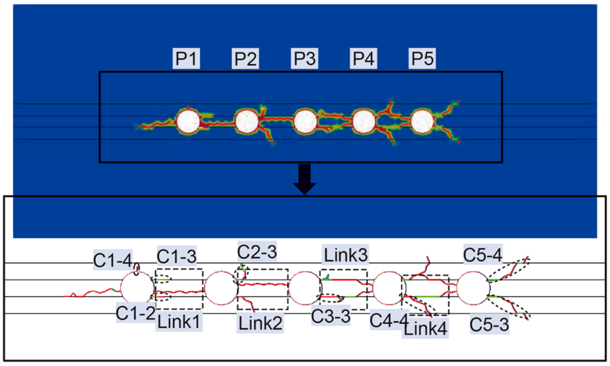

(c) Fracturing stage 3

Fig. 9. Propagation and extension process of hydraulic fracture in the vertical plane of reservoir.

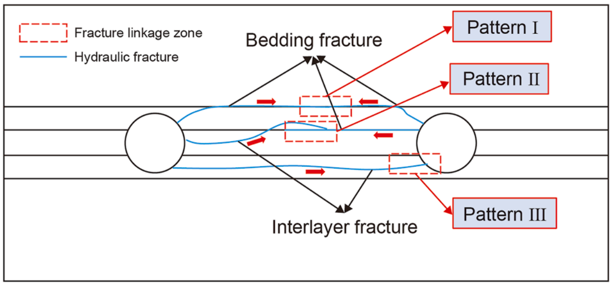

Fig. 10. Linkage model of hydraulic fractures between two adjacent perforations in the vertical plane of the layered shale reservoir.

fracturing fluid is determined based on the classic theory of on-site hydraulic fracturing failure criteria, as shown in Eq. (15):

$$P_{\text{ini}} = \sigma_{\text{t}} + 3\sigma_3 - \sigma_1 \tag{15}$$

in the equation, σ_{t} represents the tensile strength, while σ_1 and σ_3 represent the maximum and minimum principal stresses, respectively. Based on the previously mentioned vertical stress of 52 MPa and horizontal stress of 48 MPa, the calculated initiation pressure derived from the formula is 98.3 MPa. To enhance computational efficiency, the fracturing fluid pressure is set at 100 MPa in this simulation.

4.2.2. Numerical simulation results

Through numerical simulation, the propagation patterns of hydraulic fractures in the vertical plane during the staged fracturing process of a horizontal well, as well as the formation of fracture networks between different perforations, were obtained. The specific results are shown in Fig. 9. In Fig. 9, the perforation center and its surrounding fracture area in the upper part represent the fluid pressure. In the lower part, the perforation center and the surrounding colored fractures in the local enlarged view represent the fracture types. Tensile-dominated fractures (Mode I) are marked in red, shear-dominated fractures (Mode II) in yellow, and mixed-mode fractures in blue.

Fig. 9 illustrates the propagation and intersection of hydraulic fractures from each perforation in the vertical plane of the rock layer during the staged fracturing process of a horizontal well. The perforations are numbered from left to right as P1 to P5, and the primary fractures generated by each perforation are sequentially numbered as 1, 2, 3, etc., as shown in Fig. 9(a). Each primary fracture from a perforation is assigned a unique number, such as “C1-1,” “C5-2,” etc. Analysis of the overall shape of the hydraulic fractures shows that the fractures generated by each perforation intersect with the fractures from adjacent perforations during propagation and ultimately connect to form a fracture network zone, as shown in Fig. 9(b). This fracture network zone is sequentially numbered from left to right as link1 to link4.

Fig. 9(a) shows the initiation stage of hydraulic fractures from each perforation. During this stage, the primary fractures around the perforations initiate independently. Some of them are bedding fractures that extend along the bedding planes, such as C4-1, C4-2, C5-1, C5-2, etc. These bedding fractures begin to form the main fractures under the advantage of flow along the bedding planes. There are also interlayer fractures that directly propagate in the matrix between bedding planes, such as C1-4, C2-1, C2-3, C3-1, C4-3, etc. These interlayer fractures are less affected by the fractures. As the fracturing process continues, bedding fractures and interlayer fractures will interconnect to form a fracture network. For example, as shown in Fig. 9(c), the fracture link zones link1 and link2 are directly interconnected by interlayer fractures C2-1 and C3-1 with adjacent fractures; the fracture link zone link3 is formed by the interconnection of bedding fractures C3-3 and C4-1; and the fracture link zone link4 is formed by the interconnection of interlayer fractures C4-4 and C5-1.

4.2.3. Validation of the hydraulic fracturing model

The initiation pressures of the five perforations in the numerical simulation are all close to the theoretical value of 98.3 MPa and do not exceed 100 MPa, with the error range controlled between 0.20% and 1.63%. The initiation pressure of perforation P1 is the lowest, while that of perforation P5 is the highest, showing a gradual increase from the near-end perforations to the far-end perforations. This variation is related to the differences in local stress distribution at the perforation locations: as fracturing fluid is injected, the far-end perforations are more significantly affected by the cumulative effect of fluid pressure and interference from adjacent fractures, resulting in slightly higher initiation pressures. Additionally, the heterogeneity of the bedding planes and the dynamic adjustment of the stress field in the model further exacerbate the differences between the perforations. The high degree of agreement between the simulation results and the theoretical values (maximum error < 2%) validates the accuracy of the finite discrete element model.

4.2.4. Fracture linking patterns between perforations

Through the analysis of fracture network formation in laminated shale reservoirs (Fig. 10), three main fracture linking patterns between perforations were identified. The first pattern involves limited self-linking within bedding fractures, forming a confined mesh-like structure. The second pattern creates a larger fracture network through composite interconnections between interlayer and bedding fractures. The third pattern shows single fracture propagation induced by perforations, with limited networking. Importantly, the vertical extension of interlayer fractures during hydraulic fracturing is crucial for forming large-

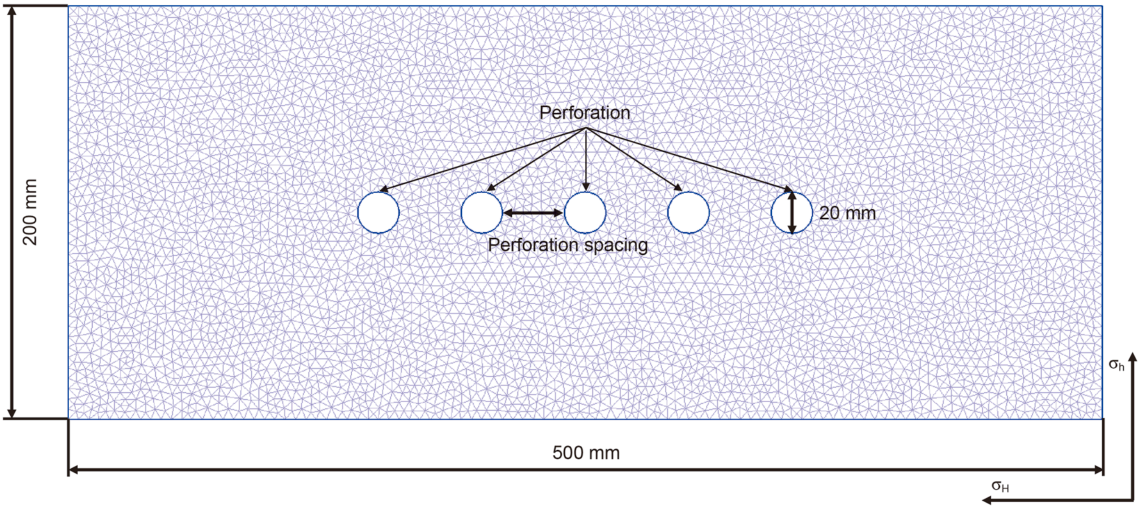

Fig. 11. Numerical model of horizontal section of staged fracturing of horizontal wells in shale formations.

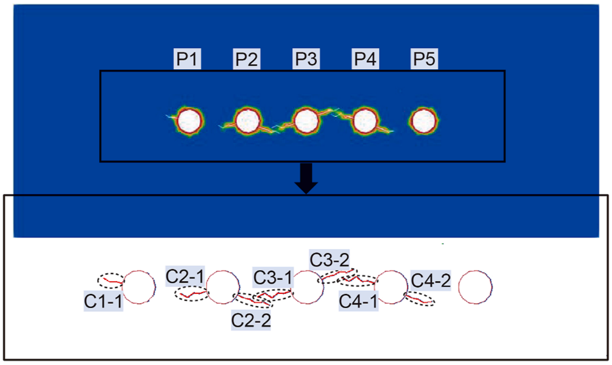

(a) Fracturing stage 1

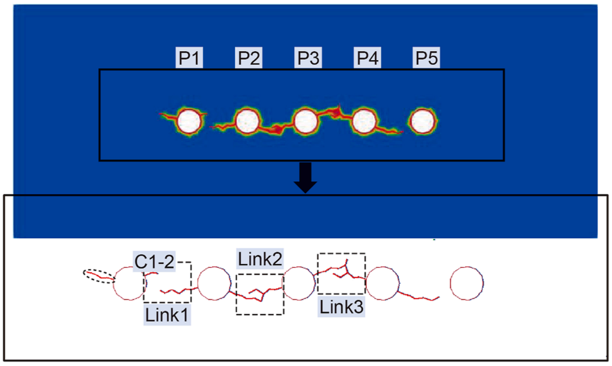

(b) Fracturing stage 2

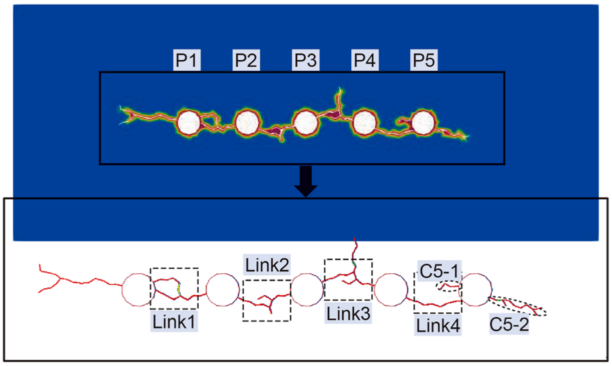

(c) Fracturing stage 3

Fig. 12. Expansion and extension process of hydraulic fractures in the horizontal plane of rock strata.

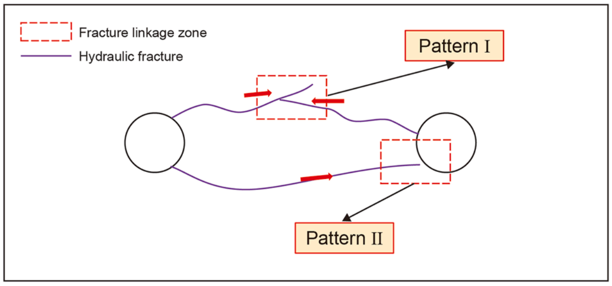

Fig. 13. Link mode of hydraulic fractures between two adjacent perforations in the shale reservoir horizontal plane.

scale networks, as it increases contact with bedding planes and promotes the development of secondary fractures, enhancing the overall complexity of the fracture network.

4.3. The propagation and distribution of hydraulic fractures in the horizontal direction of shale reservoirs

4.3.1. Establishment of numerical models

As shown in Fig. 11, the simulation model represents the horizontal section of the shale layer during the staged fracturing process of a horizontal well. The purpose of this model is to simulate the propagation and characteristics of hydraulic fractures in the horizontal plane parallel to the bedding direction within the horizontal well. The model size is 500 mm × 200 mm, consistent with the previously mentioned model. Since this plane is parallel to the bedding planes, there are no bedding planes in the model, and the micro-scale parameters are set consistently with the previous model. The generation and simulation methods for the perforation clusters are the same as those used for the vertical section model in Section 4.2. The geostress state in the model is horizontal stress, with parameters selected from the Longmaxi Formation in the horizontal section of Well H, specifically the maximum horizontal principal stress $S_{\mathrm{H}} = 55$ MPa and the minimum horizontal principal stress $S_{\mathrm{h}} = 41$ MPa. Additionally, the fracturing fluid pressure is the same as in Section 4.2, set at 100 MPa.

4.3.2. Numerical simulation results

Fig. 12 illustrates that during the initial fracturing phase, most perforations generate independent hydraulic fractures, with some producing one or two fractures. Perforation P5 does not generate any fractures at this stage, indicating that the initiation and propagation of hydraulic fractures from different perforations are not synchronized. This is because the fluid pressure initially acts only within a limited range around each perforation, with minimal impact on adjacent perforations. The behavior of hydraulic fracture initiation and propagation is primarily controlled by the local fluid pressure and the material properties of the surrounding medium.

As the fracturing process continues, the independent fractures generated by each perforation begin to extend continuously. As shown in Fig. 12(b), the majority of these fractures propagate in the direction of the maximum principal stress. When these fractures extend to the vicinity of adjacent perforations, they start to influence the hydraulic fractures of neighboring perforations, leading to the interconnection of primary fractures between adjacent perforations. For example, fracture C2-2 extends towards and meets fracture C3-1, forming fracture link zone link2. Similarly, fracture C3-2 meets and connects with fracture C4-1, forming fracture link zone link3.

In the subsequent fracturing process, new fracture link zones continue to form. For instance, fracture link zone link4 in Fig. 12(c) is formed by the direct extension of hydraulic fracture C4-2 to perforation P5, which induces the generation of new hydraulic fractures C5-1 and C5-2 at perforation P5. Meanwhile, the fracture extending from perforation P2 reaches near perforation P1. Eventually, as hydraulic fractures continue to propagate, more fractures interconnect to form additional fracture link zones.

4.3.3. Validation of the hydraulic fracturing model

In the horizontal direction numerical simulation, the initiation pressures of the five perforations are all close to the theoretical value of 98.3 MPa and do not exceed 100 MPa, with the error range controlled between 0.31% and 1.53%. The initiation pressure of perforation P1 is the lowest, while that of perforation P5 is the

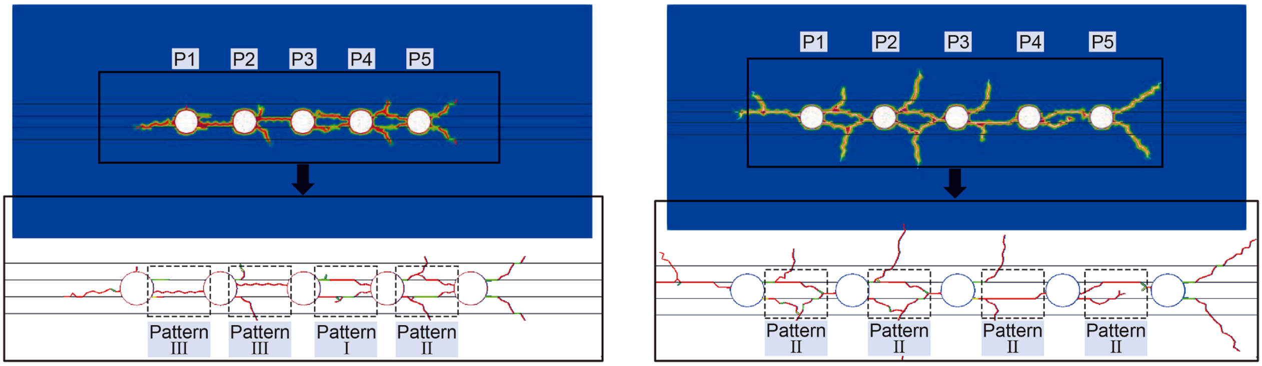

(a) Perforation spacing 50 mm

(b) Perforation spacing 62.5 mm

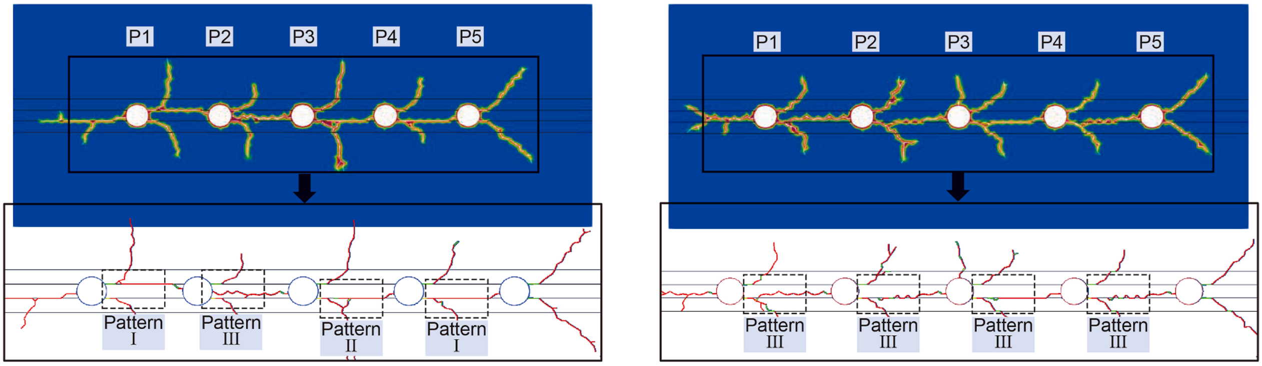

(c) Perforation spacing 71.4 mm

(d) Perforation spacing 83.3 mm

Fig. 14. Propagation patterns of hydraulic fractures with different perforation spacing in the vertical plane of the reservoir.

highest, showing a gradual increase from the near-end to the far-end. The minor deviation between the simulation results and the theoretical values (maximum error < 1.6%) validates the reliability of the finite discrete element model in simulating horizontal fracture propagation.

4.3.4. *Fracture linking patterns between perforations*

Based on the spatial propagation patterns of hydraulic fractures shown in Fig. 13, two main fracture linking modes between perforations can be identified: Pattern I, where multiple independent fractures from a single perforation intersect to form a mesh-like structure, and Pattern II, where fractures extend directly from one perforation to an adjacent unactivated perforation, forming a single linkage channel.

Numerical simulations indicate that Pattern I is dominant in the fracture system. Pattern II occurs under two conditions: the fracture path must be confined within the spatial envelope of the adjacent perforation, and the target perforation must not have initiated effective fractures in the extension direction.

Fracture linkage is controlled by the interaction of geostress and fluid stress fields. The maximum principal stress direction initially guides fracture propagation. However, as fracturing fluid is injected, the fluid stress field extends beyond the fracture tip. When fluid pressures from adjacent perforations intersect before physical fracture contact, it redirects the fracture tip stress field, inducing fracture deflection and ultimately achieving linkage between adjacent perforations.

4.4. *The impact of perforation spacing on hydraulic fracture networks*

This section focuses on the impact of perforation spacing on fracturing effectiveness. Through numerical simulations, we analyze the propagation characteristics of hydraulic fractures, the structure of fracture networks, and the mechanisms influencing fracture complexity for perforation spacings of 50, 62.5, 71.4, and 83.3 mm. By comparing fracture morphology, fluid pressure distribution, and stimulated reservoir volume under different perforation spacings, we reveal the optimal patterns for suppressing fracture competition and promoting coordinated fracture propagation.

Fig. 14 illustrates the inter-perforation hydraulic fracture linkage characteristics in the reservoir vertical plane under perforation spacings of 50, 62.5, 71.4, and 83.3 mm. Overall, the hydraulic fracture patterns vary significantly among the different spacings: At 50 mm spacing, multiple fracture modes coexist (a mix of modes I, II, and III), with mode III (dominated by single fractures) being predominant. The strong local stress interference leads to disordered fracture trajectories and fewer effective fracture networks. At 62.5 mm spacing, Mode II dominates, with complete interconnection of fractures between adjacent perforations, forming a distinct fracture network with significantly increased branch density and spatial complexity. The perforation spacing matches the stress perturbation field, and the dynamic superposition of fluid pressure and stress reorientation at the fracture tips work in tandem. At 71.4 mm spacing, modes I, II, and III coexist, with Mode III being more prominent. The fluid-stress coupling weakens, reducing the formation rate of fracture networks. At 83.3 mm spacing, isolated fracture clusters of Mode II are observed, with fracture trajectories controlled by the maximum horizontal principal stress. The stress interference effect is significantly reduced, and the inter-fracture coupling is low, preventing the formation of an effective fracture network, resulting in only single interconnected fractures.

For engineering optimization recommendations, a perforation spacing of 62.5 mm (16 perforations per meter) maximizes fracture network connectivity through the synergistic action of stress interference and fluid pressure fields. It is the optimal solution for balancing engineering controllability and reservoir stimulation efficiency.

5. Conclusions

This study systematically analyzed the initiation and propagation mechanisms of hydraulic fractures under mixed-mode effects and revealed the key laws for optimizing shale reservoir fracturing design through theoretical derivation and numerical simulation. The main achievements are as follows:

(1) Quantitative models for the plastic zone at the fracture tip were developed using the modified Mohr-Coulomb criterion, the maximum circumferential tensile stress (MCTS) criterion, and the MCTS criterion considering T-stress. These models account for shale anisotropy and reveal the influence of T-stress on plastic zone evolution.
(2) The MCTS criterion results in a larger plastic zone compared to the modified Mohr-Coulomb criterion. The plastic zone symmetry is distorted with increasing Mode II stress components. Lower tensile-to-compressive strength ratios lead to larger plastic zones, while higher tensile strength reduces the plastic zone size. T-stress significantly affects the plastic zone size, expanding it when positive and contracting it when negative.
(3) In the vertical direction, fractures form complex networks through the interconnection of bedding and interlayer fractures, with vertical interlayer fracture extension being a key factor. In the horizontal direction, fractures initially propagate independently and later interconnect under the influence of the maximum principal stress, forming mesh-like structures.
(4) Perforation spacing affects fracture behavior. At 50 mm spacing, connectivity is poor. At 62.5 mm spacing, Mode II dominance optimizes network connectivity. At 71.4 mm spacing, efficiency is reduced. At 83.3 mm spacing, isolated fractures form. Optimization shows that 62.5 mm spacing maximizes network complexity and reservoir stimulation through dynamic coupling, balancing controllability and efficiency.
(5) Based on the findings, a perforation spacing of 62.5 mm is recommended for horizontal well fracturing in shale reservoirs to enhance fracture network complexity and reservoir permeability.

CRediT authorship contribution statement

Yu Suo: Methodology, Investigation, Formal analysis, Conceptualization. **Xian-Hang Wei:** Writing – original draft, Methodology, Investigation, Formal analysis, Data curation, Conceptualization. **Yan-Jie Zhao:** Investigation. **Ying-Jie Wei:** Data curation. **Shuo Miao:** Investigation. **Yang Zhao:** Methodology. **You-Qing Zhu:** Resources. **Bin Huang:** Supervision.

Data availability statement

The data used to support the findings of this study are all shown in uploaded manuscript. Data are available from the corresponding author upon reasonable request.

Declaration of competing interest

The authors declare that they have no known competing financial interests or personal relationships that could have appeared to influence the work reported in this paper.

Acknowledgement

The work presented in this paper was financially supported by the First-Class Discipline Collaborative Innovation Program of Heilongjiang Province (Grant No. LJGXCG2024-F02) and the Key Research and Development Program of Heilongjiang Province (Grant No. 2024ZX09C01). The Postdoctoral Special Funding of Heilongjiang Province (LBH-TZ2301) is also gratefully acknowledged and supported by Heilongjiang Provincial Natural Science Foundation of China (LH2022E020).

References

Aliha, M.R.M., Ayatollahi, M.R., Smith, D.J., et al., 2010. Geometry and size effects on fracture trajectory in a limestone rock under mixed-mode loading. Eng. Fract. Mech. 77 (11), 2200–2212. https://doi.org/10.1016/j.engfracmech.2010.03.037.
Cao, Z.C., Chen, Q., Cui, J.Y., et al., 2024. Simulation of field-scale hydraulic fracture propagation mechanism based on extended finite element method. Drill. Eng. 51 (5), 85–92. https://doi.org/10.12143/j.ztgc.2024.05.010 (in Chinese).
Chen, M., 2013. Mechanism of hydraulic fracture deflection and propagation in shale gas reservoirs. J. China Univ. Pet. (Nat. Sci. Ed.) 37 (5), 88–94. https://doi.org/10.3969/i.issn.1673–5005.2013.05.013 (in Chinese).
Cotterell, B., Rice, J.R., 1980. Slightly curved or kinked cracks. Int. J. Fract. 16 (2), 155–168. https://doi.org/10.1007/BF00012619.
Cui, Z., Hou, B., 2023. Criteria for discriminating layer-penetration fracturing considering pressure drop and interfaces. Eng. Fract. Mech. 292, 109622. https://doi.org/10.1016/j.engfracmech.2023.109622.
Cui, Z., Hou, B., 2024a. Numerical investigation of mode I fracture toughness anisotropy of deeply textured shale. Geoenergy Sci. Eng. 237, 212820. https://doi.org/10.1016/j.geoen.2024.212820.
Cui, Z., Hou, B., 2024b. Mechanical behavior of mixed-mode I-II fracture in deep laminated shale based on finite discrete element method. Theor. Appl. Fract. Mech. 133, 104596. https://doi.org/10.1016/j.tafmec.2024.104596.
Erdogan, F., Sih, G.C., 1963. On the crack extension in plates under plane loading and transverse shear. ASME J. Basic Eng. 85 (4), 519–525. https://doi.org/10.1115/1.3656897.
Fatahi, H., Hossain, M.M., Sarmadivaleh, M., 2017. Numerical and experimental investigation of the interaction of natural and propagated hydraulic fractures. J. Nat. Gas Sci. Eng. 37, 409–424. https://doi.org/10.3390/en11102541.
Gao, W., Cui, S., Xiao, T., et al., 2021. Initiation law of rock cracks based on minimum plastic zone radius criterion. J. Coal 46 (10), 3193–3202. https://doi.org/10.13225/j.cnki.jccs.2020.0938 (in Chinese).
Hu, R.L., Huang, P.Y., Zheng, S.C., 2010. Theoretical derivation of fracture process zone size in concrete. Eng. Mech. 27 (6), 127–132 (in Chinese).
Kang, D., Chung, Y.K., Wei, W., et al., 2018. DEM modeling of hydraulic fracturing in permeable rock: influence of viscosity, injection rate, and in-situ stress. Acta Geotech 13 (5), 1187–1202. https://doi.org/10.1007/s11440–018–0627–8.
Li, H.F., Xing, C.F., Li, X., 2014. Fracture characteristics of inclined cracks in rock mass under uniaxial compression. J. Water Resour. Archit. Eng. 12 (3), 1–4. https://doi.org/10.3969/j.issn.1672–1144.2014.03.001 (in Chinese).
Li, P.T., Wang, Y.Q., Liu, J.Q., Liang, M.X., 2025. Evaluation of carbon emission efficiency and analysis of influencing factors of Chinese oil and gas enterprises. Energy Sci. Eng. 13 (3), 1156–1170. https://doi.org/10.1002/ese3.2055.
Li, Y.M., Si, N., Lv, W., et al., 2019. Study on complex fracture networks in shale fracturing based on discrete element numerical method. Drill. Prod. Tech 42 (1), 46–49. https://doi.org/10.3969/J.ISSN.1006–768X.2019.01.14 (in Chinese).
Liu, H.B., 2018. Crack Propagation Law of Rock-like Materials with Prefabricated Cracks and Application of 3D Printing Technology. PhD Dissertation. China University of Mining and Technology, Beijing (in Chinese).
Liu, H.Y., 2019. Initiation mechanism of compression-shear cracks in rocks considering T-stress. J. Geotech. Eng. 41 (7), 1296–1302. https://doi.org/10.11779/CJGE201907014 (in Chinese).
Liu, Y., He, P.T., Zhao, M.J., 2006. Study on rock failure mechanism based on damage-fracture theory. J. Undergr. Space Eng. (6), 1076–1080 (in Chinese).
Munjiza, A., 2004. The Combined Finite-Discrete Element Method. John Wiley & Sons, Chichester.
Sousa, R.A., Castro, J.T.P., Lopes, A.A.O., et al., 2013. On improved crack tip plastic zone estimates based on T-stress and on complete stress fields. Fatig. Fract. Eng. Mater. Struct. 36 (1), 25–38. https://doi.org/10.1111/j.1460–2695.2012.01684.x.
Tang, S.B., Liu, X.J., Luo, J., et al., 2017. Theoretical model study on hydraulic pressure-induced tensile and shear rupture of fractures. J. Rock Mech. Eng. 36 (9), 2124–2135. https://doi.org/10.13722/j.cnki.jrme.2017.0114 (in Chinese).
Wang, Q., Wang, Y.F., Hu, Y.Q., et al., 2024. Propagation and interference law of zipper fracturing fractures in deep shale gas wells. Petrol. Explor. Dev. 51 (5), 1141–1149. https://doi.org/10.11698/PED.20240603 (in Chinese).
Wang, Q., Wang, Y.F., Sun, Y., et al., 2025. Interference law of zipper fracturing fractures in deep shale gas wells influenced by small faults. Nat. Gas Geosci. 36 (2), 342–353. https://doi.org/10.11764/j.issn.1672–1926.2024.07.008 (in Chinese).

Wang, S., Chen, M., Lv, J.X., et al., 2024. Fiber optic strain evolution characteristics induced by hydraulic fracture propagation in horizontal wells affecting adjacent vertical wells. J. Northwest. Polytech. Univ. 48 (4), 100–141. https://doi.org/10.3969/j.issn.2095–4107.2024.04.008 (in Chinese).

Wang, S.F., Tan, F., Lv, J.H., et al., 2021. Discrete element numerical simulation of hydraulic fracturing based on Hoek-Brown strength criterion. J. Wuhan Univ. (Nat. Sci. Ed.) 54 (4), 290–297. https://doi.org/10.14188/j.1671–8844.2021–04–002 (in Chinese).

Wang, T., Zhou, W., Chen, J., et al., 2014. Simulation of hydraulic fracturing using particle flow method and application in a coal mine. Int. J. Coal Geol. 121, 113. https://doi.org/10.1016/j.coal.2013.10.012.

Wei, M.D., Dai, F., Xu, N.W., et al., 2017. Fracture prediction of rocks under mode I and mode II loading using the generalized maximum tangential strain criterion. Eng. Fract. Mech. 186, 21–38. https://doi.org/10.1016/j.engfracmech.2017.09.001.

Wu, X., Li, X., 1989. Analysis and modification of fracture criteria for mixed-mode crack. Eng. Fract. Mech. 34 (1), 55–64. https://doi.org/10.1016/0013–7944(89)90242–7.

Xu, Z., Xie, X., Kong, X.W., et al., 2025. Influence analysis of bedding angles on hydraulic fracture propagation in coal rock. Coal Mine Saf. 1–9. https://doi.org/10.13347/j.cnki.mkaq.20231905 (in Chinese).

Yan, C.Z., Zheng, H., 2016a. Multi-well hydraulic fracturing simulation based on FDEM-Flow. J. Yangtze River Sci. Res. Inst. 33 (7), 63–67. https://doi.org/10.11988/ckyyb.20150234 (in Chinese).

Yan, C.Z., Zheng, H., 2016b. Influence of heterogeneity on hydraulic fracturing based on FDEM-flow method. J. Undergr. Space Eng. 12 (S2), 625–638 (in Chinese).

Yan, C.Z., Zheng, H., Sun, G.H., et al., 2016. Influence of in-situ stress on hydraulic fracturing based on FDEM-flow. Rock Soil Mech. 37 (1), 237–246. https://doi.org/10.16285/j.rsm.2016.01.028 (in Chinese).

Yang, D.P., Pan, H.Y., Zhang, P.P., et al., 2017. Study on plastic zone of 3D fatigue elastic-plastic curved cracks. Mech Q. 38 (4), 667–674. https://doi.org/10.15959/j.cnki.0254–0053.2017.04.007 (in Chinese).

Yang, D.P., Wang, S.Q., Zhou, C., et al., 2019. Crack opening displacement of 3D quasi-static elastic-plastic curved cracks. J. Mech. Strength 41 (2), 442–446. https://doi.org/10.16579/j.issn.1001.9669.2019.02.030 (in Chinese).

Zhang, H.W., Zhou, C.H., He, J., et al., 2025. DEM-based coupling simulation method for pressure relief mining via hydraulic fracturing in hard roof. J. Coal 1–12. https://doi.org/10.13225/j.cnki.jccs.2024.1118 (in Chinese).

Zhang, J.W., Liu, X.J., Xiong, J., et al., 2023. Hydraulic fracture propagation law and main controlling factors in conglomerate based on discrete element method. Daqing Pet. Geol. Dev. 42 (3), 48–57. https://doi.org/10.19597/j.issn.1000–3754.202204056 (in Chinese).

Zhang, Y.H., Yang, Y.K., Wang, C.L., 2024. Multi-fracture cross-layer propagation law of hydraulic fracturing in fragmented soft coal seam roof. Coal Mine Saf. 55 (12), 63–71. https://doi.org/10.13347/j.cnki.mkaq.20231310 (in Chinese).

Zuo, T., Li, Y.Y., Zhang, M.Y., et al., 2025. Numerical simulation of fluid injection schemes on hydraulic fracture propagation. Pet. Geol. Eng. 39 (1), 114–122 (in Chinese).